MINISTRY OF EDUCATION AND TRAINING

VIETNAM ACADEMY OF SCIENCE AND TECHNOLOGY

GRADUATE UNIVERSITY OF SCIENCE AND TECHNOLOGY

LE THI THANH TAM

DEVELOPMENT OF BIOCOMPATIBLE NANOFLUIDS AS EFFECTIVE CONTRAST AGENTS FOR MRI AND CT IMAGING

SUMMARY OF DISSERTATION ON SCIENCES OF MATTER

Major: Inorganic Chemistry

Code: 9 44 01 13

Ha Noi – 2025

The dissertation is completed at: Department of Materials and Electrical Engineering, Institute of Materials Science, Vietnam Academy Science and Technology

Supervisors:

1. Supervisors 1: Assoc.Prof. Dr. Le Trong Lu, Institute of Materials Science, Vietnam Academy Science and Technology.
2. Supervisors 2: Prof. Dr. Le Anh Tuan, Phenikaa University.

Referee 1: Assoc.Prof. Dr. Nguyen Hoang Nam, University of Science, Vietnam National University.

Referee 2: Assoc.Prof. Dr. Tran Dang Thanh, Institute of Materials Science, Vietnam Academy Science and Technology.

The dissertation is examined by Examination Board of Graduate University of Science and Technology, Vietnam Academy of Science and Technology at 9:00 a.m. on November 21, 2025.

The dissertation can be found at:

1. Graduate University of Science and Technology Library
2. National Library of Vietnam

INTRODUCTION

1. The urgency of the PhD thesis

In contemporary medicine, the ability to detect diseases at an early stage, provide accurate diagnoses, and effectively monitor disease progression, particularly in the case of cancer, is of paramount importance for improving therapeutic outcomes and patient prognosis. Among the various imaging modalities, magnetic resonance imaging (MRI) and computed tomography (CT) are recognized as two cornerstone techniques, owing to their capability to deliver high spatial resolution images, excellent tissue contrast, and deep penetration into internal anatomical structures without invasive intervention. Nevertheless, both MRI and CT have inherent limitations in detecting early–stage lesions with high sensitivity. This shortcoming necessitates the administration of contrast agents to amplify signal differences between tissues and thereby improve diagnostic accuracy.

Clinically, MRI contrast agents are predominantly gadolinium(III)–based complexes (e.g., gadopentetate dimeglumine, gadoterate meglumine), which function by shortening the longitudinal relaxation time (T_1) to produce brighter signals (positive contrast) on MRI scans. However, these agents exhibit low magnetic susceptibility, require relatively high dosages, and carry potential risks associated with the release of toxic Gd^{3+} ions, in addition to increasing diagnostic costs. For CT, iodine-based contrast agents provide strong X–ray attenuation but suffer from short circulation times, rapid renal clearance, poor accumulation at target lesions, and the potential to cause severe adverse reactions, including anaphylaxis.

Given these limitations, biocompatible nanofluids, defined as stable aqueous dispersions of inorganic nanoparticles with proven biosafety, have emerged as promising candidates for next–generation contrast agents. By tailoring particle size, composition, and surface chemistry through precise control of synthesis parameters, such nanofluid systems can be engineered to enhance biocompatibility, improve contrast efficiency, and extend their applicability to MRI, CT, or even integrated multimodal imaging platforms within a single formulation.

Motivated by these considerations, the present research *"**Development of biocompatible nanofluids as effective contrast agents for MRI and CT imaging**"* was undertaken. This study focuses on the design and synthesis of

novel nanofluid systems with potential utility as high–performance contrast agents. The fabrication process employs straightforward wet–chemical techniques, enabling precise control over particle size and composition, thereby allowing the fine–tuning of biocompatibility and imaging properties for specific diagnostic requirements. Importantly, these materials also demonstrate the potential for multimodal diagnostic functionality, offering a pathway toward the development of next–generation contrast agents with superior safety profiles and enhanced diagnostic performance in modern medical practice.

2. The research objectives

Synthesis of a series of highly biocompatible nanofluid systems based on inorganic oxide nanomaterials, Fe_3O_4, Gd_2O_3 and Bi_2O_3, capable of enhancing image contrast in MRI and CT diagnostic applications.

3. The main research content

1. Synthesis of composite nanofluid systems (Fe_3O_4/Gd_2O_3, Bi/Bi_2O_3, Bi_2O_3/Gd_2O_3) with excellent aqueous dispersibility via wet–chemical methods.
2. Preliminary assessment of the cytotoxicity of the synthesized fabricated nanofluids through *in vitro* experiments.
3. Investigation of the contrast enhancement performance of the synthesized nanofluids for MRI techniques (T_1 positive contrast, T_2 negative contrast, dual-mode T_1-T_2 contrast), CT imaging and multimodal MRI/CT imaging diagnostics.

CHAPTER 1. OVERVIEW

1.1. Contrast agents for MRI and CT Imaging

MRI and CT are two modern medical imaging modalities that are widely employed in disease diagnosis, particularly in oncology. Both techniques often require the use of contrast agents to enhance soft tissue resolution, improve sensitivity, and increase specificity. Conventional contrast agents, such as Gd–chelates for MRI and iodine–based compounds for CT, have demonstrated clinical effectiveness; however, they suffer from major limitations, including short blood circulation times, non–selective tumor distribution, poor drug–loading capacity, and potential toxicity risks.

Nanomaterials offer promising solutions to these limitations. Their nanoscale dimensions enable tissue penetration, while the enhanced permeability and retention (EPR) effect facilitates passive tumor targeting. Furthermore, surface modification allows for conjugation with targeting ligands or therapeutic agents, and the incorporation of multifunctionality (e.g., multimodal imaging, drug delivery, photothermal conversion) into a single nanoplatform.

1.2. Magnetic Resonance Imaging (MRI)

1.2.1. Principles of MRI Imaging

MRI operates on the principle of nuclear magnetic resonance of protons in a strong magnetic field under high frequency radiofrequency (RF) excitation. When the RF pulse is switched off, protons relax back to their equilibrium state through two mechanisms: longitudinal relaxation (T_1) and transverse relaxation (T_2). Differences in T_1 and T_2 between tissues generate image contrast. MRI contrast agents function by shortening either T_1 or T_2 of protons, producing hyperintense signals (T_1 positive contrast agents) or hypointense signals (T_2 negative contrast agents) in the resulting images. Their effectiveness is quantified by the longitudinal relaxivity (r_1) and transverse relaxivity (r_1) values ($mM^{-1}s^{-1}$), with the r_2/r_1 ratio determining the appropriate imaging mode.

1.2.2. Inorganic nanomaterials for MRI imaging

T_1 contrast agents typically contain paramagnetic ions with large magnetic moments, most notably Gd^{3+}, which can efficiently shorten the longitudinal relaxation time (T_1) of protons, thereby generating bright, high contrast images. Commercial Gd–chelates are generally considered safe due to their stable chelating structures, which limit the presence of free Gd^{3+} ions. Nevertheless, they still pose a potential risk of Gd^{3+} release and have relatively low contrast enhancement efficiency. To address these issues, ultrasmall Gd_2O_3 nanoparticles (<3 nm) coated with biocompatible polymers such as PMAO, PEG, or dextran have been developed. These nanoparticles exhibit higher r_1 values, better stability, and lower toxicity owing to their large surface area, which enhances proton interaction and reduces inner–sphere water diffusion limitations.

In contrast, T_2 contrast agents such as Fe_3O_4 or $MnFe_2O_4$ nanoparticles generate strong local magnetic field inhomogeneities, accelerating transverse

relaxation (T_2) and producing characteristic dark regions in MRI scans. These agents are particularly useful for detecting lesions in organs such as the liver and spleen. However, their main drawbacks include susceptibility to imaging artifacts and difficulty in differentiating whether signal attenuation is due to pathology or the presence of the agent itself.

Dual-mode contrast agents combine the advantages of both T_1 and T_2 imaging, enabling simultaneous bright–dark visualization and cross–validation for improved diagnostic accuracy. Hybrid nanostructures integrating Gd^{3+} and Fe_3O_4, or core–shell architectures such as Fe_3O_4@Gd_2O_3, have been investigated, offering strong contrast effects in both imaging modes. Nonetheless, optimizing their size and structure to minimize antagonistic interactions between the two imaging mechanisms remains a significant challenge.

1.3. Computed Tomography (CT)

1.3.1. Principles of CT Imaging

CT imaging is based on the attenuation of X–ray beams as they pass through tissues, which depends on tissue density, atomic number (Z), thickness, and the X–ray beam energy. The attenuation coefficient (μ) increases with higher atomic number and decreases as the X–ray energy increases.

1.3.2. Inorganic nanomaterials for CT imaging

Due to its limited soft–tissue discrimination, CT often requires contrast agents, most commonly iodine–based contrast agents (IBCA). While these agents improve image contrast, they have notable drawbacks, including adverse side effects, short circulation times, unsuitability for patients with renal impairment, and poor biodegradability.

Nanomaterials containing high–Z elements (e.g., Au, Bi, Ta) have emerged as promising CT contrast agents owing to their strong X–ray attenuation, ability to be functionalized for drug delivery and targeting, and potential for multifunctionality. For example, gold nanoparticles (AuNPs) can increase CT signals by approximately 2.5 times compared to iodine agents, though their cost is high. Bismuth oxide (Bi_2O_3) nanoparticles exhibit high X–ray attenuation efficiency, lower toxicity, and lower cost than AuNPs. Gadolinium oxide (Gd_2O_3) nanoparticles can enhance both CT and MRI contrast due to their high atomic number and large magnetic moment,

especially when polymer–functionalized to improve aqueous dispersibility and reduce toxicity.

1.4. Inorganic nanomaterials as multimodal MRI/CT contrast agents

There is a growing trend toward integrating the advantages of multiple imaging modalities:

Approach 1: Incorporating distinct contrast enhancing components within a single nanoparticle (e.g., Fe_3O_4/Au or Gd_2O_3/Au) to simultaneously improve MRI and CT contrast.

Approach 2: Utilizing intrinsically multifunctional nanomaterials, such as Gd–containing nanoparticles, which inherently provide dual MRI/CT contrast enhancement, …

1.5. Methods for nanofluid fabrication

Nanomaterial synthesis methods: thermal decomposition and polyol processes.

Nanoparticle surface modification methods: ligand–exchange strategies and coating with silica or amphiphilic polymers.

CHAPTER 2. EXPERIMENTAL

2.1. Synthesis of Fe_3O_4/Gd_2O_3@PMAO nanoparticles (GFO@PMAO)

Fe_3O_4/Gd_2O_3 nanoparticles were synthesized via a thermal decomposition method in octadecene solvent, using various Gd^{3+}/Fe^{3+} molar ratios. The as-prepared nanoparticles were subsequently surface modified by coating with poly(maleic anhydride–alt–1–octadecene) (PMAO), allowing the nanoparticles to disperse stably in aqueous media.

2.2. Synthesis of Bi/Bi_2O_3@PAA nanoparticles

Bi/Bi_2O_3 nanoparticles were prepared via thermal decomposition in a mixed solvent system of octadecene and dibenzyl ether. Surface modification was achieved through a ligand–exchange process using poly(acrylic acid) (PAA), thereby imparting excellent aqueous dispersibility to the nanoparticles.

2.3. Synthesis of Bi_2O_3/Gd_2O_3@PEI nanoparticles

Bi_2O_3/Gd_2O_3@PEI nanoparticles were synthesized via the polyol method, with polyethyleneimine (PEI) present during synthesis both to control particle formation and to provide a biocompatible surface coating, ensuring stable dispersion in water.

2.4. Characterization techniques

Transmission Electron Microscopy (TEM) and Scanning Electron Microscopy (SEM)

X–ray Diffraction (XRD)

Energy dispersive X-ray (EDX)

X–ray Photoelectron Spectroscopy (XPS)

Vibrating Sample Magnetometry (VSM)

Ultraviolet–Visible Absorption Spectroscopy (UV–Vis)

Fourier–Transform Infrared Spectroscopy (FT–IR)

Thermogravimetric Analysis (TGA)

Dynamic Light Scattering (DLS)

Inductively Coupled Plasma Mass Spectrometry (ICP–MS)

2.5. *In vitro* cytotoxicity assay

The cytotoxicity of the nanofluid contrast agents was assessed in Vero and Hep–G2 cell lines using the MTT assay.

2.6. Evaluation of MRI and CT contrast enhancement performance

In vitro and *in vivo* MRI image measurements of the contrast agent samples were performed on a Siemens MAGNETOM Avanto 1.5 Tesla MRI scanner.

In vitro and *in vivo* CT image measurements were carried out using a 128-Somatom Perspective CT scanner (Siemens, Germany). The acquired imaging data were processed and analyzed using the syngo CT VC30 – easyIQ software package.

CHAPTER 3. Fe_3O_4/Gd_2O_3@PMAO NANOPARTICLES AS T_1-T_2 DUAL-MODE CONTRAST AGENTS FOR MRI DIAGNOSTICS

3.1. Characterization of Fe_3O_4/Gd_2O_3 nanoparticles (GFO NPs)

TEM images revealed that the molar ratio of Gd^{3+}/Fe^{3+} had a pronounced influence on the morphology and particle size of the nanoparticles (Figure 3.1). In the Fe_3O_4 sample, the particles exhibited a uniform spherical morphology with an average diameter of 8.5 ± 0.6 nm. Upon the introduction of Gd^{3+} at low concentrations (10–20 mol%), the particle size increased to 12–14.5 nm, and the morphology became more diverse, including spherical, cubic, octahedral, and tetrahedral shapes. In particular, the sample containing 20 mol% Gd^{3+} predominantly displayed highly uniform cubic particles.

At a Gd^{3+} content of 30 mol%, the particle morphology tended to revert to spherical, with an average size of approximately 10 nm but with reduced uniformity. At high Gd^{3+} concentrations (70–100 mol%), all particles were spherical, and their size decreased sharply from 10 nm to only 1.5–3 nm.

This morphological evolution can be attributed to the substitution of Fe^{3+} ions (0.67 Å) with larger Gd^{3+} ions (0.94 Å), which causes lattice expansion and promotes crystal growth at low Gd^{3+} concentrations. In contrast, at high Gd^{3+} content, the stronger Gd-O bond energy compared to Fe-O slows down the crystal growth process, leading to smaller particle sizes.

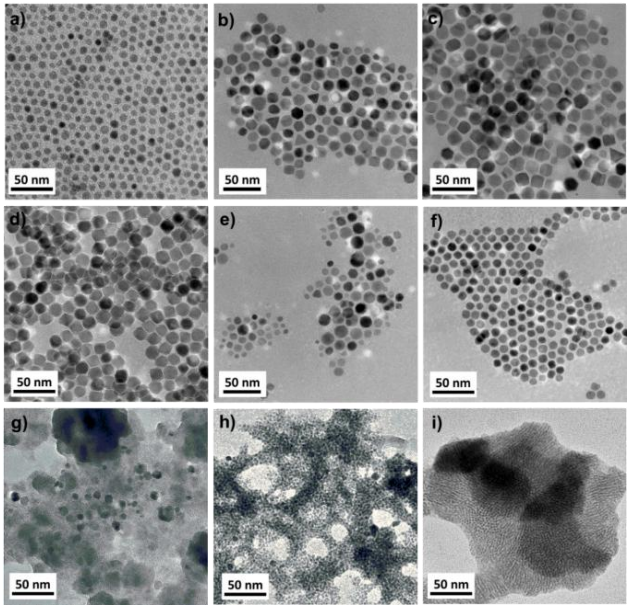

Figure 3.1. TEM images of GFO NPs at various Gd^{3+}/Fe^{3+} molar ratios: 0/10 (a), 1/9 (b), 1.5/8.5 (c), 2/8 (d), 3/7 (e), 7/3 (f), 8/2 (g), 9/1 (h) and 10/0 (i).

XRD results showed that that samples with $Gd^{3+} \leq 30$ mol% exhibited a single–phase cubic spinel structure (Fd-3m), with the lattice constant increasing from 8.341 to 8.365 Å and crystallite size from 8.9 to 13.1 nm, in agreement with TEM results. At $Gd^{3+} > 30\%$, the crystallinity decreased, diffraction peaks broadened, and structural features approached those of Gd_2O_3 (a = 10.8 Å), indicating lattice distortion and phase transition due to octahedral site saturation, cation imbalance, and Gd^{3+} ions accumulation outside the crystal lattice.

VSM results showed all samples to be superparamagnetic or soft–magnetic at room temperature. M_s increased from 59.65 to 68.3 emu/g as Gd^{3+} content rose from 0 to 20 mol%, attributed to larger crystallite size and sustained A–B superexchange interactions. For Gd^{3+} content exceeded 30%, M_s dropped sharply to 2–3 emu/g, with nearly linear magnetization curves, reflecting the near–paramagnetic behavior of Gd_2O_3. This reduction in magnetization arose from spinel lattice cation imbalance, reduced A–B exchange pairs, and spin disorder.

Table 3.1. Structural parameters and magnetic properties of GFO NPs.

Sample	D_{TEM} (nm)	a (Å)	D_{XRD} (nm)	M_S (emu/g)	Mr (emu/g)	H_C (Oe)
Fe_3O_4	8,5±0,5	8,341±0,001	8,9±0,1	59,65	0,37	7,45
GFO-1/9	12±1,4	8,342±0,0015	10±0,2	63,72	1,62	18,99
GFO-1.5/8.5	14,5±1,5	8,353±0,002	13,1±0,5	65,90	0,97	10,61
GFO-2/8	14,5±1,1	8,365±0,001	12,3±0,2	68,30	1,16	13,33
GFO-3/7	9,9±2,9	8,347±0,0015	11,2±0,3	55,93	1,65	19,13
GFO-7/3	10,1±0,7	10,499±0,038	1,27±0,07	10,37	0,14	12,78
GFO-8/2	~8	10,643±0,017	1,08±0,03	3,09	0,11	20,27
GFO-9/1	3,1±0,45	10,627±0,016	1,39±0,03	2,71	0,15	27,18
Gd_2O_3	1,5±0,21	10,821±0,019	1,28±0,02	1,76	0,0095	4,43

ICP–MS results indicated that the Gd/Fe molar ratios in the NPs were lower than those in the precursors, suggesting a lower reaction efficiency for Gd^{3+} compared to Fe^{3+}. Among the samples, GFO–7/3 was selected for further investigation.

TEM images (Figure 3.2) showed GFO-7/3 NPs with uniform morphology and an average diameter of 10.1 ± 0.7 nm. HRTEM revealed a lattice spacing of 2.46 Å, corresponding to the (222) plane of Fe_3O_4 but slightly larger than the standard value, indicating lattice expansion due to Fe^{3+} substitution by Gd^{3+}. SAED patterns confirmed a polycrystalline structure with both Fe_3O_4 and Gd_2O_3 phases. The Fe_3O_4 phase displayed (311), (400), (422), (440), and (533) planes with enlarged d–spacings, while the Gd_2O_3 phase showed (222) and (622) planes, indicating that part of the Gd^{3+} did not incorporate into the spinel lattice but formed a separate oxide

phase. These results reflect two concurrent mechanisms: (i) Gd^{3+} doping into the Fe_3O_4 lattice, causing crystal distortion, and (ii) Gd_2O_3 phase formation when the structural tolerance limit is exceeded.

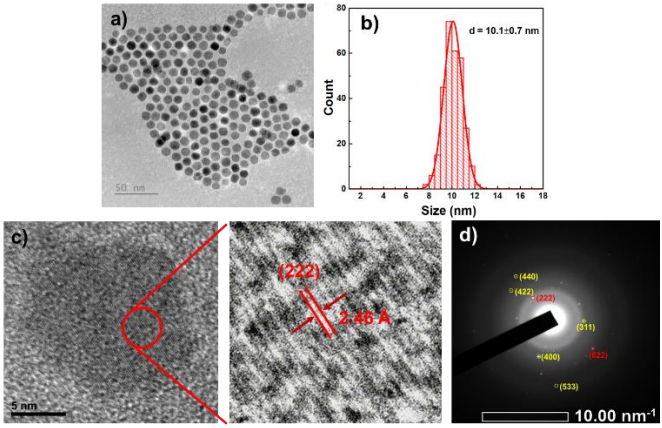

Figure 3.2. TEM image (a), size distribution histogram (b), HRTEM image(c) and SAED pattern (d) of the GFO-7/3 NPs.

XPS analysis confirmed the presence of C, N, O, Fe, and Gd elements. The Fe2p spectrum revealed both Fe^{2+} and Fe^{3+} states, characterized by the main peaks and Fe^{3+} satellite features. The Gd4d spectrum exhibited two peaks corresponding to the +3 oxidation state of Gd^{3+}. The O1s spectrum comprised three components: 530.4 eV (lattice oxygen in the spinel structure), 528.5 eV (lattice oxygen at particle interfaces or grain boundaries), and 532.0 eV (hydroxyl groups and adsorbed water).

3.2. Characterization of GFO@PMAO NPs

FT-IR spectra confirmed the successful coating of GFO NPs with PMAO. TGA analysis indicated that the PMAO shell accounted for 63.9% of the total weight, while the GFO core represented 36.1% (Figure 3.3a,b).

Dynamic light scattering (DLS) and zeta potential measurements showed a hydrodynamic diameter of 58.7 nm and a zeta potential of -63.4 mV, indicating excellent colloidal stability primarily due to electrostatic repulsion between negatively charged particles (Figure 3.3c,d). Moreover, GFO@PMAO NPs maintained stable size and zeta potential for a long time (>2 months), was stable in the pH range of 2–13 and salt solutions with concentrations up to 0.45 M, demonstrating superior colloidal stability and adaptability under various physiological conditions.

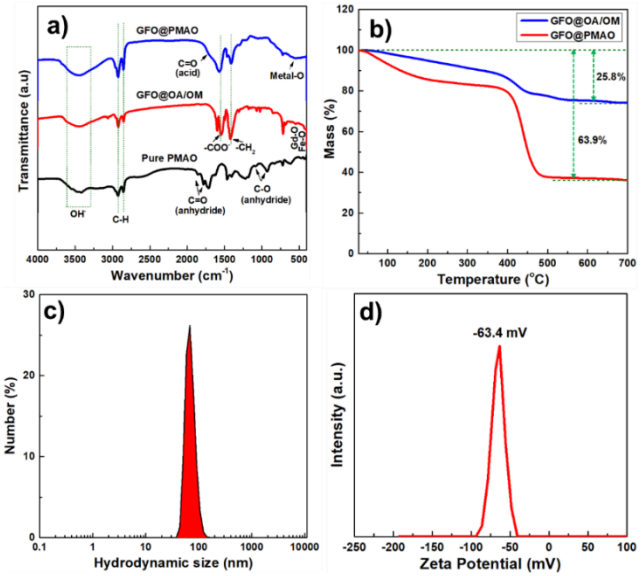

Figure 3.3. (a) FT-IR spectra, (b) TGA scans of GFO NPs before and after encapsulation with PMAO, (c) DLS pattern and (d) zeta potential of the GFO@PMAO NPs.

3.3. In vitro cytotoxicity assay

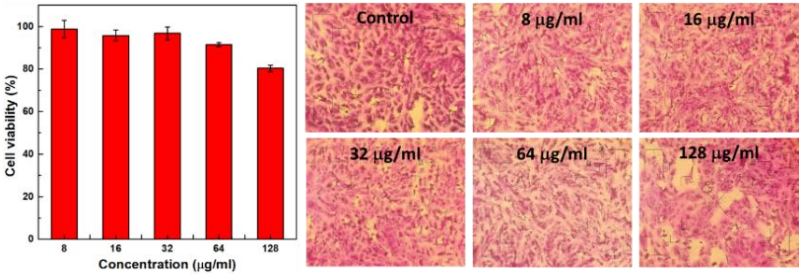

Figure 3.4. MTT assay of Vero cell viability after incubation with different concentrations of GFO@PMAO CNPs for 48h.

The MTT assay on Vero cells revealed that GFO@PMAO NPs caused no morphological changes and maintained >80% cell viability at concentrations up to 128 μg/mL after 48 h, indicating low cytotoxicity. This biocompatibility is attributed to the PMAO coating, which minimizes direct interactions between the inorganic core and cells. Furthermore, Fe incorporation further enhanced the biocompatibility, highlighting the promise of GFO@PMAO NPs for biomedical applications.

3.4. *In vitro* and *in vivo* MR Imaging

The GFO@PMAO NPs exhibited concentration-dependent dual contrast behavior on a 1.5 T clinical MRI scanner, with T_1W signal enhancement and T_2W signal attenuation as the (Gd+Fe) concentration increased from 0.0625 to 0.8 mM. The determined r_1 and r_2 values were 18.20 $mM^{-1}s^{-1}$ and 94.75 $mM^{-1}s^{-1}$, yielding an r_2/r_1 ratio of 5.21, which is ideal for T_1-T_2 dual-mode imaging. These values surpass those of many reported Fe- and Gd-based agents, with r_1 about four times higher than commercial T_1 agents (Dotarem, Magnevist, Gadovist) and r_2 comparable to Ferumoxytol. The high relaxivity is attributed to the synergistic effects of Fe and Gd, whereby Gd^{3+} ions incorporated into the Fe_3O_4 lattice enhance the T_2 effect through spin–magnetization alignment, while ultrasmall surface Gd_2O_3 domains facilitate water exchange for strong T_1 enhancement, further complemented by partial T_1 shortening from the iron oxide core.

Table 3.2. Relaxivities of GFO NPs at different Gd/Fe ratios.

Sample	Longitudinal relaxivity, r_1 ($mM^{-1}s^{-1}$)	Transverse relaxivity, r_2 ($mM^{-1}s^{-1}$)	r_2/r_1
Fe_3O_4	3,32±0,21	119,39±3,45	35,96
GFO-1/9	5,91±0,21	165,36±4,11	27,98
GFO-2/8	7,66±0,37	189,80±6,31	24,78
GFO-3/7	1,54±0,13	92,02±3,27	59,75
GFO-7/3	18,20±1,25	94,75±6,29	5,21
GFO-8/2	19,53±1,82	67,15±2,32	3,44
GFO-9/1	20,45±2,03	54,60±1,78	2,67
Gd_2O_3	20,31±1,97	33,54±1,84	1,65

The MRI performance of GFO@PMAO NPs with varying Gd/Fe ratios was systematically evaluated. The r_1 value increased slightly at Gd^{3+} contents ≤ 20%, decreased sharply at 30% Gd^{3+}, and then rose markedly again when Gd^{3+} exceeded 30%, reaching a maximum of 20.45 $mM^{-1}s^{-1}$ for the GFO-9/1 sample. In contrast, r_2 increased at Gd contents ≤ 20% (189.8 $mM^{-1}s^{-1}$) and then dropped markedly when Gd exceeded 30% (33.54 $mM^{-1}s^{-1}$ for Gd_2O_3).

Overall, the GFO sample with a Gd/Fe ratio of 7/3 achieved the most balanced r_1 and r_2 values, resulting in the best overall MRI performance. The contrast enhancement mechanism is attributed to the synergistic effects of ultrasmall Gd_2O_3 domains and Gd doping, which enhance r_1 via inner-sphere relaxation; the superparamagnetic Fe_3O_4 core, which enhances r_2 via outer-sphere relaxation; and the PMAO coating, which preserves efficient surface water exchange.

In vivo MRI of rabbits after intravenous administration of GFO@PMAO NPs ([Gd+Fe] = 0.045 M) revealed a pronounced increase in T_1W liver signal intensity (ΔSNR ~93.3% at 60 min, decreasing to 82.1% at 90 min) accompanied by a corresponding decrease in T_2W signal intensity (ΔSNR ~58.7% at 60 min, decreasing to 49.8% at 90 min) (Figure 3.5). The contrast effects peaked at approximately 60 min post-injection and then slightly declined at 90 min, suggesting partial clearance or metabolism from the liver. No adverse effects were observed during a one-month follow-up, indicating that GFO@PMAO not only provides dual-mode *in vivo* contrast enhancement but also exhibits excellent biocompatibility.

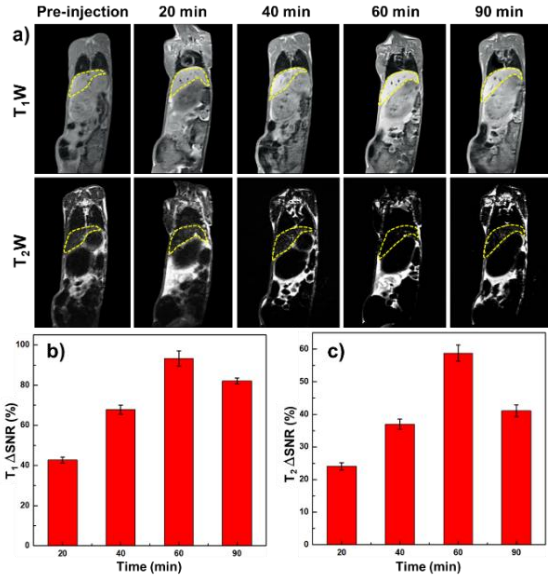

Figure 3.5. (a) T_1W and T_2W MRI images of rabbits before and after intravenous injection of GFO@PMAO NPs; (b) ΔSNR in liver of T_1-weighted and (c) T_2-weighted images after administration (n = 2).

CHAPTER 4. ULTRASMALL Bi/Bi_2O_3 NANOPARTICLES AS CONTRAST AGENT FOR CT IMAGING DIAGNOSTICS

4.1. Characterization of Bi/Bi_2O_3 NPs

In this study, ultra-small Bi/Bi_2O_3 NPs were synthesized via a one-step thermal decomposition method, employing $Bi(NO_3)_3$ as the precursor in an ODE/BDE solvent mixture, with the presence of oleic acid (OA) and oleylamine (OM) as surfactants, with OM also acting as a reducing agent. The OA/OM ratio was found to be a key factor controlling the oxidation state and phase composition: OA-rich conditions favored Bi_2O_3 formation, OM-rich conditions yielded metallic Bi. An intermediate OA/OM ratio of 2:1 produces hybrid Bi/Bi_2O_3 NPs with an average diameter of approximately 3 nm, uniform size distribution, and high colloidal stability. TEM, HRTEM, XRD, and Rietveld refinement analyses confirmed a high-crystallinity core–shell structure with a metallic Bi core and a Bi_2O_3 shell, comprising 75.1% Bi and Bi_2O_3 (Figure 4.1).

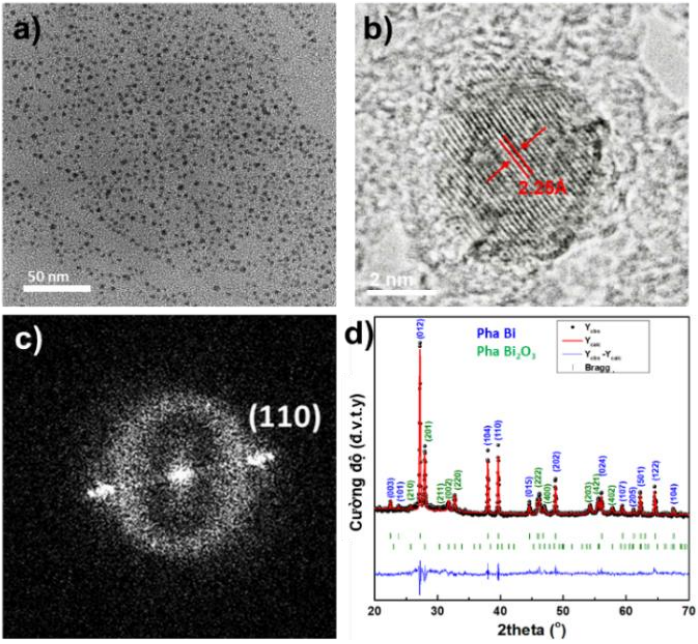

Figure. 4.1. a) TEM image, b) size distribution of Bi/Bi_2O_3 NPs, c) HRTEM image of Bi/Bi_2O_3 NPs with an inset FFT image and d) Rietveld refinement profile of XRD data of as prepared Bi/Bi_2O_3 NPs.

UV–Vis spectroscopy showed a characteristic Bi_2O_3 absorption at 273 nm and an optical band gap of 3.88 eV, indicating quantum confinement. EDX and elemental mapping revealed homogeneous Bi and O distribution, and XPS confirmed the coexistence of Bi^0 and Bi^{3+} species, supporting partial surface oxidation and core–shell structure (Figure 4.2).

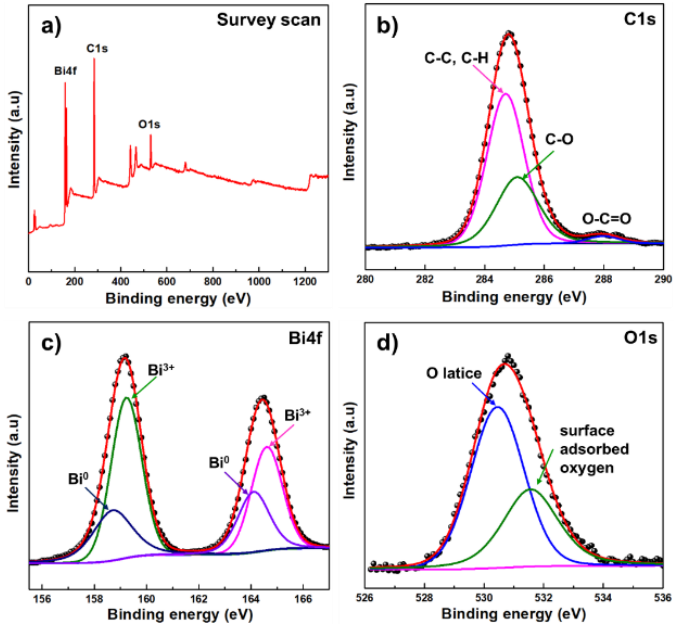

Figure 4.2. XPS spectra of Bi/Bi_2O_3 NPs: a) Scan survey; High-resolution XPS spectra of b) C1s, c) Bi4f and d) O1s.

4.2. Characterization of Bi/Bi_2O_3@PAA NPs

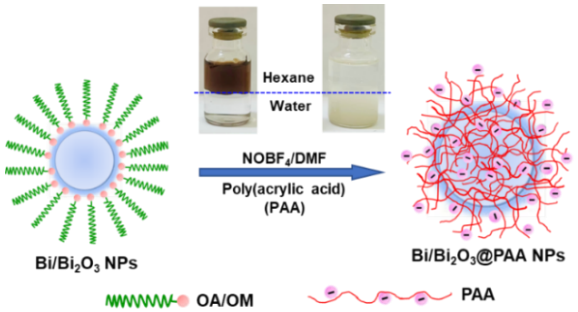

Figure 4.3. Illustration of the phase transfer of Bi/Bi_2O_3 NPs by ligand exchange method.

Hydrophobic Bi/Bi_2O_3 NPs were rendered hydrophilic via poly(acrylic acid) (PAA) surface functionalization through an OA/OLA ligand-exchange process, resulting in enhanced dispersibility in aqueous media (Figure 4.3).

FT-IR spectra and TGA analysis confirmed the stable covalent attachment of PAA chains onto the NP surface (Figure 4.4). The resulting Bi/Bi_2O_3@PAA NPs exhibited an average hydrodynamic diameter of 36.8 nm, a zeta potential of -38.8 mV, remarkable colloidal stability across a wide pH range (2–12), and no precipitation after two months of storage.

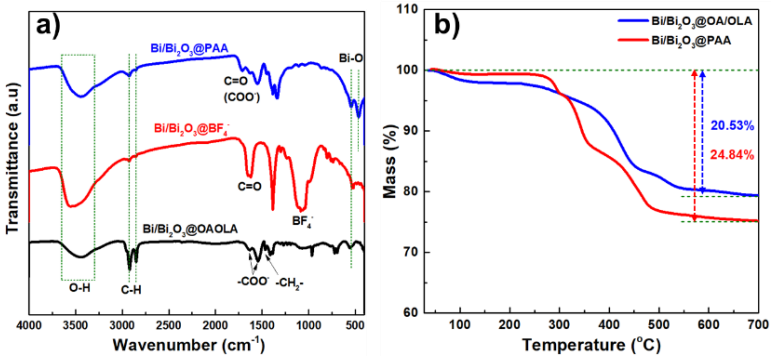

Figure 4.4. FTIR spectra and b) TGA plots of Bi/Bi_2O_3 NPs before surface modification (Bi/Bi_2O_3@OA/OLA) and after modification with PAA.

4.3. *In vitro* toxicity assessment

The biocompatibility of Bi/Bi_2O_3@PAA NPs was evaluated through MTT assay, measuring the viability of Vero cells after 72 hours of incubation with varying NP concentrations (Figure. 4.5). The results demonstrated that cell viability remained above 72% even at concentrations as high as 200 µg/mL, indicating low cytotoxicity and suitable biocompatibility of the NPs for potential *in vivo* CT applications.

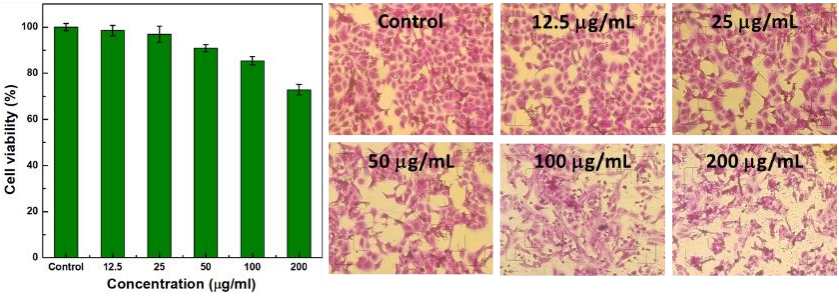

Figure 4.5. Cellular cytotoxicity in Vero cells after 72hours incubation.

4.4. Performance on CT imaging *in vitro*

In vitro CT phantom imaging demonstrated that Bi/Bi_2O_3@PAA NPs produced a concentration-dependent enhancement in X-ray attenuation, with CT values increasing linearly with Bi concentration (slope: 14,32 $HU.mM^{-1}$ at 80 kV), surpassing several iodine-based clinical and reported Bi-based agents. The CT numbers remained relatively stable across tube voltages of 80–130 kV, owing to the high K-edge energy of Bi (90.5 keV), indicating superior and voltage-independent CT imaging performance.

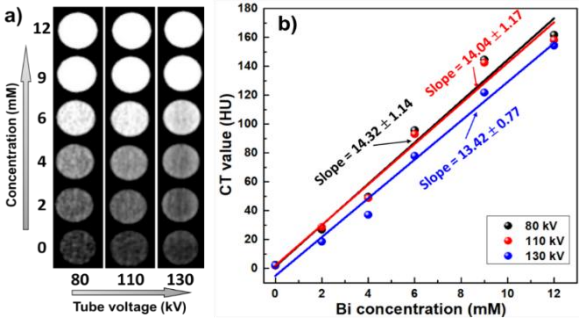

Figure 4.6. *In vitro* CT images and b) corresponding CT signals curves of Bi/Bi_2O_3@PAA with different concentration under different tube ranging from 80 to 130 kV.

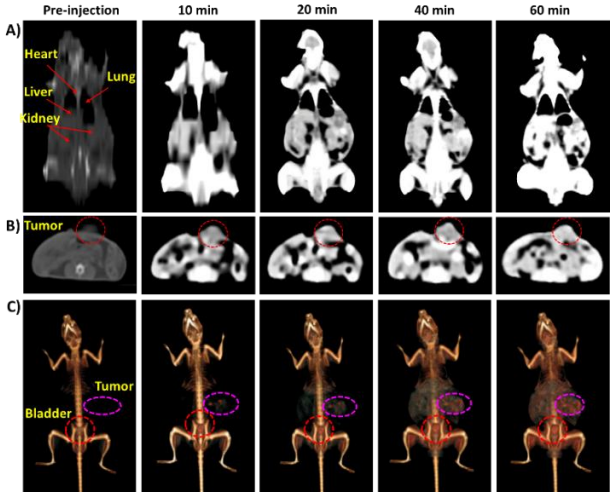

Figure 4.7. CT images of Sarcoma 180 tumor-bearing mice: pre- and post-treatment by intraperitoneal injection of Bi/Bi_2O_3@PAA NPs: A) Coronal section, B) Axial section of the tumor region, C) 3D renderings whole-body.

CHAPTER 5. Bi_2O_3/Gd_2O_3@PEI NANOPARTICLES AS CONTRAST AGENTS FOR MULTIMODAL MRI/CT IMAGING DIAGNOSTICS

5.1. Characterization of Bi_2O_3/Gd_2O_3@PEI NPs

In this work, Bi_2O_3/Gd_2O_3@PEI nanoparticles (BGO@PEI NPs) were synthesized via a polyol process in ethylene glycol, with polyethylenimine (PEI) functioning as both a size-control agent and a biocompatible coating. Precursor Bi^{3+}/Gd^{3+} molar ratios of 3/7, 5/5, 6/4, 7/3, 8/2, and 10/0 were explored to assess the effect of composition on morphology and structure. The BGO-5/5 sample, with a uniform average diameter of ~5.8 nm, was selected for further investigation.

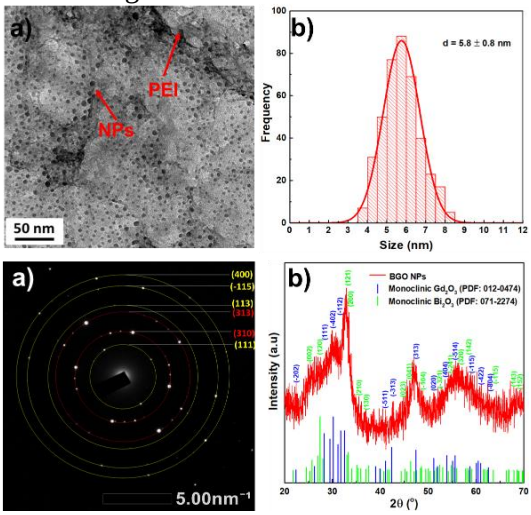

Figure 5.1. a) TEM image, b) size distribution histogram, c) SEAD pattern, and d) XRD pattern of BGO@PEI NPs.

TEM, SAED and XRD analyses confirmed that the NPs were spherical and composed of coexisting Bi_2O_3 and Gd_2O_3 crystalline phases (Figure 5.1). XPS results further verified the oxidation states of Bi^{3+} and Gd^{3+}, the presence of PEI amino groups, lattice oxygen, and oxygen vacancies. EDS and ICP-MS results demonstrated the homogeneous distribution of Bi, Gd, and O throughout the NPs, with an actual Bi/Gd molar ratio of 1.73, higher than the nominal value, attributable to the lower reaction efficiency of Gd^{3+}.

FTIR analysis revealed the characteristic vibrational bands of PEI, while TGA determined that the oxide core accounted for approximately 72% of the total mass. DLS measurements showed a hydrodynamic diameter of ~91.6

nm and a zeta potential of +62.8 mV, indicating excellent colloidal stability of the BGO@PEI nanoparticles in aqueous media (Figure 5.2).

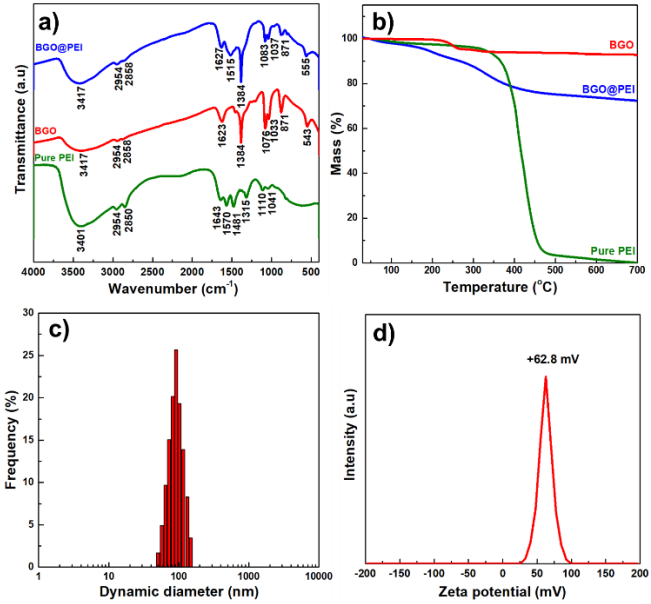

Figure 5.2. a) FTIR spectra, b) TGA plot, c) DLS spectrum and d) zeta potential of BGO@PEI NPs.

5.3. *In vitro* cytotoxicity assay

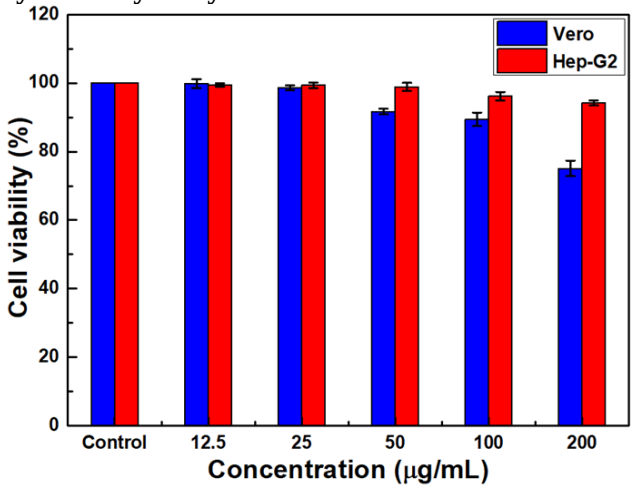

Figure 5.3. MTT assay of Vero and Hep-G2 cell viability after 48 hours incubation with different concentrations of BGO@PEI NPs.

In vitro cytotoxicity evaluation of BGO@PEI on human liver cancer cells (Hep-G2) and normal Vero cells over a concentration range of 0–200 µg/mL for 48 hours demonstrated low toxicity of the material. Specifically, at the highest concentration (200 µg/mL), cell viability remained at 94% for Hep-G2 and 75% for Vero cells, indicating only a mild impact on normal cells under prolonged exposure.

5.4. *In vitro* and *in vivo* MR/CT Imaging

5.4.1. In vitro MR/CT images

The *in vitro* MRI results demonstrat that BGO@PEI NPs exhibited outstanding T_1-weighted MRI contrast enhancement, with a longitudinal relaxivity (r_1) of 16.52 $mM^{-1}s^{-1}$ at 1.5 T, approximately four times higher than that of Gd-DTPA. This high r_1 value enabled bright T_1-weighted imaging even at low concentrations. The superior T_1 contrast is attributed to the combination of a high surface density of Gd^{3+} ions, small particle size (~5.8 nm), and PEI coating, which promotes aqueous dispersion, increases water-proton accessibility, and optimizes inner-sphere relaxation interactions.

For CT phantom imaging, BGO@PEI NPS containing both Bi (Z = 83) and Gd (Z = 64) exhibited strong X-ray attenuation. The CT attenuation increased linearly with (Bi+Gd) concentration, yielding a slope of 16.59 $HU.mM^{-1}$ at 80 kV, approximately 3-4 times higher than iodine-based contrast agents (e.g., Ultravist). The highest attenuation was observed at 80 kV, near the Bi K-edge, and although slightly reduced at higher voltages, BGO@PEI NPs maintained superior X-ray attenuation across clinically relevant scanning conditions.

5.4.2. In vivo MR/CT images

In vivo CT imaging of Sarcoma 180 tumor-bearing mice after intraperitoneal injection of BGO@PEI NPs ([Bi+Gd] = 26,4 mM) showed a significant increase in CT values at the tumor site, from 21.5 HU pre-injection to 80.4 HU at 60 min post-injection, representing nearly a fourfold enhancement. This result confirms efficient tumor accumulation via the enhanced permeability and retention (EPR) effect. Compared to previously studied Bi/Bi_2O_3@PAA NPs, BGO@PEI NPs exhibited higher ΔHU values, attributable to the synergistic Bi_2O_3-Gd_2O_3 composite structure and PEI coating, which improved intratumoral distribution and retention.

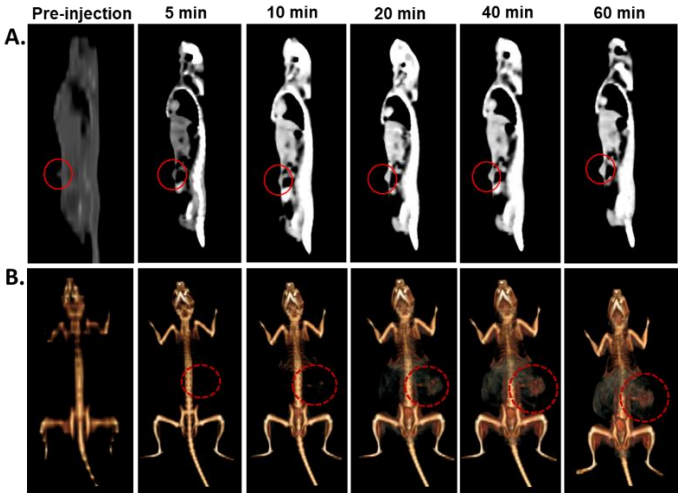

Figure 5.4. CT images of Sarcoma 180 tumor-bearing mice: pre- and post-treatment by intraperitoneal injection of BGO@PEI NPs: A) Sagittal section, B) 3D renderings whole-body.

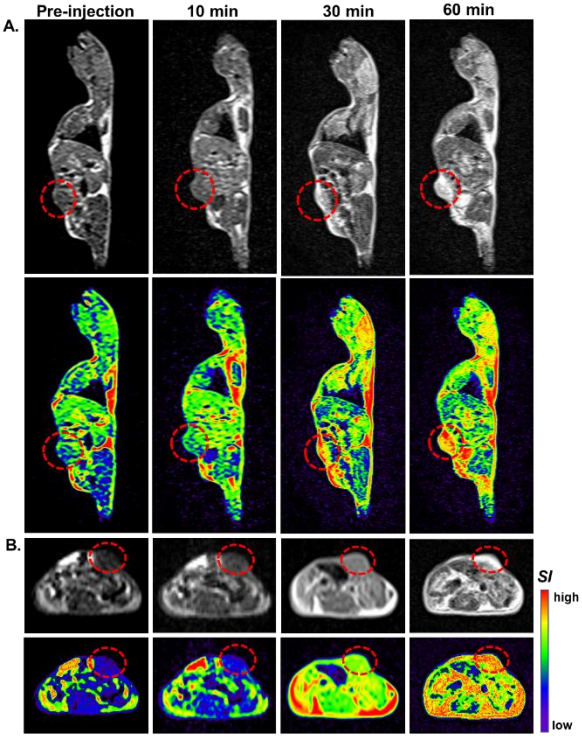

Figure 5.5. T_1W-MRI images of Sarcoma 180 tumor-bearing mice: pre- and post-treatment by intraperitoneal injection of BGO@PEI NPs: A) Sagittal section, B) Axial section of the tumor region.

In vivo T_1-weighted MRI revealed a marked increase in tumor signal intensity over time. At 60 min post-injection, the ΔSNR increased by 67% in sagittal slices and 75% in axial slices. The observed T_1 brightening reflects both effective nanoparticle accumulation in the tumor and the strong T_1-shortening capability of Gd^{3+} ions within the nanostructure.

Overall, BGO@PEI NPs functions as an effective dual-modal MRI/CT contrast agent, providing clear imaging at low concentrations, high X-ray attenuation, and sustained tumor signal enhancement suitable for non-invasive diagnostics. The combined presence of two high-Z elements (Bi and Gd) along with PEI coating confers advantages in both contrast efficiency and colloidal stability, highlighting their potential for multimodal imaging and tumor progression monitoring.

CONCLUSIONS AND RECOMMENDATIONS

I. Conclusions

The dissertation successfully synthesized several highly biocompatible nanofluid systems based on inorganic oxide nanomaterials, including Fe_3O_4, Gd_2O_3, and Bi_2O_3, and comprehensively evaluated their potential as novel contrast agents for MRI and CT imaging. Through systematic synthesis, surface modification, and characterization of their structural, physicochemical, biological, and imaging enhancement properties, the following significant results were achieved:

1. For Fe_3O_4/Gd_2O_3 nanoparticles (GFO NPs), spherical and monodisperse nanoparticles with an average size of ~10 nm were successfully synthesized. After surface modification with PMAO, the GFO@PMAO NPs exhibited excellent aqueous dispersibility and high biocompatibility, maintaining over 80% cell viability at a concentration of 128 μg/mL. *In vitro* MRI measurements revealed r_1=18.20 $mM^{-1}s^{-1}$, r_2=94.75 $mM^{-1}s^{-1}$, and an r_2/r_1 ratio of 5.21, indicating dual-mode T_1–T_2 contrast capability. *In vivo* MRI studies on rabbits demonstrated pronounced signal enhancement in the liver in both T_1W and T_2W images, confirming the material's efficiency as a dual-mode MRI contrast agent.

2. Ultra-small Bi/Bi_2O_3 NPs (~3 nm) were successfully synthesized with controlled Bi_2O_3 shell formation by adjusting the OA/OM ratio. Surface modification with PAA yielded Bi/ Bi_2O_3@PAA NPs with excellent aqueous dispersibility and long-term colloidal stability. *In vitro* cytotoxicity evaluation using Vero cells indicated good biocompatibility, maintaining over 72% cell viability even at a high concentration of 200 μg/mL. Due to the high Bi content and ultrasmall particle size, the Bi/Bi_2O_3 NPs showed superior X-ray attenuation performance, achieving 14.32 HU.mM^{-1}, surpassing that of commercial iodine-based agents. *In vivo* CT imaging on mice demonstrated significant signal enhancement in the liver, kidneys, and bladder, with tumor accumulation reaching ΔHU = 53.6 HU after 60 min, highlighting its potential for tumor detection and localization via CT imaging.
3. Bi_2O_3/Gd_2O_3@PEI NPs (BGO@PEI) with an average diameter of 5.8 nm were obtained via a one-step polyol method with a straightforward procedure, integrating the strong T_1 relaxivity of Gd with the high X-ray attenuation efficiency of Bi. The The BGO@PEI NPs exhibited a r_1 value of 16,52 $mM^{-1}s^{-1}$ and X-ray attenuation efficiency of 16.59 HU.mM^{-1}, demonstrating their potential for dual MRI/CT imaging. *In vivo* MRI/CT studies on mice showed marked tumor accumulation, with CT intensity increasing from 21.5 to 80.4 HU after 60 min, while the T_1-weighted MRI signal rose significantly (ΔSNR = 75%), confirming enhanced tumor visualization. Furthermore, *in vitro* cytotoxicity assays using Vero and Hep-G2 cell lines indicated good biocompatibility up to 200 μg/mL.

II. Recommendations

On that basis, we propose the following recommendations:

1. Conduct further *in vivo* studies on animal models to comprehensively evaluate contrast enhancement efficiency and biosafety of the developed nanoparticle systems.
2. Optimize multifunctional nanoparticle structures by integrating targeting ligands, therapeutic agents, or theranostic functions to expand applications in combined diagnosis and therapy.

NEW CONTRIBUTIONS OF THE PHD THESIS

- The PhD thesis successfully fabricated three advanced multifunctional hybrid nanofluid systems (Fe_3O_4/Gd_2O_3, Bi/Bi_2O_3, Bi_2O_3/Gd_2O_3) with well-controlled size, morphology, and surface properties. The as-prepared materials exhibit superior characteristics compared with several currently available commercial contrast agents.
- The PhD thesis demonstrated the effectiveness and application potential of the fabricated multifunctional nanosystems through *in vivo* animal studies, notably the Fe_3O_4/Gd_2O_3 system as a dual-mode MRI T_1-T_2 contrast agent and the Bi_2O_3/Gd_2O_3 system for combined MRI/CT imaging.

LIST OF THE PUBLICATIONS RELATED TO THE DISSERTATION

1. **Le T. T. Tam**, Nguyen T. N. Linh, Le T. Tam, Duong V. Thiet, Pham H. Nam, Nguyen T. H. Hoa, Le A. Tuan, Ngo T. Dung and Le T. Lu, "*Biocompatible PMAO-coated Gd_2O_3/Fe_3O_4 composite nanoparticles as an effective T_1–T_2 dual-mode contrast agent for magnetic resonance imaging*", Materials Advances, **2025**, 6, 1319. (Q1, IF 5.2)
2. **Le T. T. Tam**, Duong T. Ngoc, Nguyen T. N. Linh, Le T. Tam, Nguyen V. Dong, Nguyen T. Yen, Nguyen T. Suong, Ngo T. Dung and Le T. Lu, *"Ultrasmall Bi/Bi_2O_3 nanoparticles as biocompatible and efficient CT imaging contrast agents"*, Nanoscale Adv., **2025**. 7, 4183. (Q1, IF 4.7)
3. Nguyen Thi Ngoc Linh, Nguyen Hoa Du, Ngo Thanh Dung, **Le Thi Thanh Tam**, Pham Hong Nam, Phan Thi Hong Tuyet, Le Trong Lu, and Le The Tam, "*Synthesis of Fe_3O_4@Au Core–Shell Nanoparticles with Varying Thicknesses for Application in Computed Tomography Imaging*", ChemistryOpen, **2025**, e202500166. (Q2, IF 2.3)
4. Nguyen T. T. Khue, **Le T. T. Tam***, Ngo T. Dung, Nguyen T. N. Linh, Nguyen T. Dung, Le T. Tam, Le T. Lu, *"Synthesis and characterization of PVP coated gadolinium oxide nanoparticles for imaging applications"*, Vietnam journal of Science and Technology, **2024**, 62(1), 68-77. (Scopus)
5. Nguyen Thi Ngoc Linh, Le The Tam, **Le Thi Thanh Tam***, Ngo Thanh Dung, Phan Thi Hong Tuyet, Dinh Thi Truong Giang, Le Trong Lu, *"Synthesis of PAA- coated ultra-small Gd_2O_3 nanoparticles for MRI contrast agents"*, Vietnam Journal of Science and Technology, **2025**. (Accepted, Scopus).
6. Le Trong Lu, **Le Thi Thanh Tam**, Ngo Thanh Dung, Nguyen Thi Ngoc Linh, Le The Tam, Nguyen Thi Hong Hoa, Le Anh Tuan, *"Synthesis protocol for gadolinium iron oxide nanoparticles as dual-mode MRI contrast agent"*, Patent, **2025**, Intellectual Property Office of Viet Nam. Application accepted, Decision No. 43576/QĐ-SHTT dated April 8, 2025.
7. Le Trong Lu, **Le Thi Thanh Tam**, Ngo Thanh Dung, Nguyen Thi Yen, "*Method for preparing $Bi@Bi_2O_3$ core–shell nanoparticles and their application as contrast agents for CT imaging*", Patent, Intellectual Property Office of Viet Nam. Application accepted, Decision No. 157289/QĐ-SHTT dated July 30, 2025.
8. **Le T. T. Tam**, Le V. Thanh, Le G. Nam, Doan T. Tung, Hoang T. Dung, Le T. Tam, Ho D. Quang, Ngo T. Dung and Le T. Lu, *"Facile synthesis of Polyethylenimine coated Bi_2O_3/Gd_2O_3 composite nanoparticles as multimodal MRI/CT contrast agents"*, RSC Adv., **2025**, 15, 48393. (Q1, IF 4.6).